Chinese Journal of
POLYMER SCIENCE

RESEARCH ARTICLE

https://doi.org/10.1007/s10118-026-3868-2
Chinese J. Polym. Sci.

Leveraging Steric Hindrance Engineering in Conjugated Polymers for Enhanced NIR-II Fluorescence Imaging and High-efficiency Photothermal Therapy

Bin Chang[a], Chen-Hang Xi[a], Zi-Kun Yu[a], Zi-Xin Hu[a], Peng-Fei Chen[b*], Qu-Li Fan[a,c], and Peng-Fei Sun[a*]

[a] *State Key Laboratory of Flexible Electronics & Institute of Advanced Materials (IAM), Jiangsu Key Laboratory for Biosensors, Nanjing University of Posts & Telecommunications, Nanjing 210023, China*
[b] *Huangshan Technology Innovation Center for Green Chemical Engineering and New Materials, School of Chemistry and Chemical Engineering, Huangshan University, Huangshan 245041, China*
[c] *State Key Laboratory of Coordination Chemistry, School of Chemistry and Chemical Engineering, Nanjing University, Nanjing 210023, China*

Electronic Supplementary Information

Abstract The aggregation-caused quenching (ACQ) effect severely limits the fluorescence quantum yield of conventional conjugated polymers in the second near-infrared window (NIR-II). Herein, we propose an innovative steric hindrance regulation strategy by precisely controlling the topological position of alkyl side chains on acceptor units to disrupt the backbone planarity. Two donor-acceptor polymers, PBIQ and PBOQ, were synthesized *via* Stille coupling. PBIQ, featuring internal alkyl chains on the thiophene ring, exhibited remarkable aggregation-induced emission (AIE) characteristics and significantly suppressed ACQ. The prepared PBIQ nanoparticles (NPs) demonstrated high-performance NIR-II fluorescence imaging and a high signal-to-background ratio. Remarkably, under 808 nm laser irradiation, PBIQ NPs achieved an ultrahigh photothermal conversion efficiency of 70.51%, outperforming most reported organic photothermal agents. Both *in vitro* and *in vivo* studies confirmed that PBIQ NPs enable precise tumor diagnosis and efficient ablation with excellent biocompatibility. This work highlights the critical role of spatial steric hindrance in balancing radiative and nonradiative transitions, offering a promising molecular design paradigm for integrated NIR-II phototheranostics.

Keywords NIR-II fluorescence imaging; Photothermal therapy; Conjugated polymer; Steric hindrance engineering

Citation: Chang, B.; Xi, C. H.; Yu, Z. K.; Hu, Z. X.; Chen, P. F.; Fan, Q. L.; Sun, P. F. Leveraging steric hindrance engineering in conjugated polymers for enhanced NIR-II fluorescence imaging and high-efficiency photothermal therapy. *Chinese J. Polym. Sci.* https://doi.org/10.1007/s10118-026-3868-2

INTRODUCTION

The second near-infrared (NIR-II) fluorescence (FL) imaging and NIR-II photothermal therapy (PTT) are two highly complementary modalities for cancer theranostics.[1] Integrating both functions into a single NIR-II absorption agent can significantly improve the accuracy of tumor diagnosis and treatment by leveraging the high sensitivity of NIR-II FL imaging and therapeutic capability of PTT, effectively compensating for the inherent limitations of each modality. Among the NIR-II absorption materials developed for such integrated applications, conjugated polymers (CPs) are particularly promising candidates owing to their conveniently tunable photophysical properties, high photostability, and excellent biocompatibility.[2]

Among the many photothermal agents, conjugated polymers (a widely adopted strategy for designing NIR-II-absorbing CPs) involve incorporating strong electron donors and acceptors into the polymer backbone to narrow the bandgap. However, in such low-bandgap CPs, nonradiative decay pathways dominate over radiative ones, resulting in severely quenched NIR-II fluorescence.[3–5] To address this, aggregation-induced emission (AIE)-active segments or weak electron donors have been introduced to partially suppress excessive nonradiative decay and enhance NIR-II FL. Additionally, non-conjugated spacer segments have been incorporated into the polymer backbone to disrupt intermolecular π–π stacking and mitigate aggregation-caused quenching (ACQ). Despite these advances, the currently developed CPs still face critical challenges: their NIR-II fluorescence quantum yields remain generally low, and ACQ in the aggregated state continues to compromise both the imaging quality and photothermal conversion efficiency (PCE). Therefore, developing CPs that simultaneously overcome ACQ, provide bright NIR-II fluorescence, and deliver efficient photothermal conversion remains an urgent yet unmet challenge.[6–9]

Herein, we propose a molecular design strategy based on

* Corresponding authors, E-mail: iampfsun@njupt.edu.cn (P.F.C.)
E-mail: pfchen@hsu.edu.cn (P.F.S.)
Received June 29, 2026; Accepted August 28, 2026; Published online November 11, 2026

© Chinese Chemical Society
Institute of Chemistry, Chinese Academy of Sciences

the regulation of acceptor steric hindrance to address this challenge. Using QIQ-2Sn as the donor unit, two D-A type conjugated polymers, PBIQ and PBOQ, were synthesized *via* Stille coupling with the benzothiadiazole derivatives BBT (bearing a 2-ethylpentyl chain on the inner side of the thiophene ring) and BBTD (bearing a 2-octyldodecyl chain on the outer side of the thiophene ring) as the acceptor units, respectively. The core of this strategy lies in modulating molecular conformation by precisely controlling the topological position of the alkyl side chains on the acceptor unit. In PBIQ, the inner alkyl chain is positioned close to the benzothiadiazole plane, generating a significant steric hindrance effect that increases the dihedral angle between the alkylthiophene and benzothiadiazole, thereby effectively disrupting the backbone planarity and suppressing intermolecular π–π stacking in the aggregated state. In contrast, PBOQ and bearing outer alkyl chains retain better backbone planarity, and served as the controls. This structural difference directly dictates their emission behavior: PBIQ exhibits typical AIE characteristics (αAIE=1.15) with remarkably enhanced NIR-II fluorescence relative to PBOQ, whereas PBOQ still suffers from ACQ. Notably, water-soluble nanoparticles based on PBIQ (PBIQ NPs) achieved an outstanding photothermal conversion efficiency of 70.51% under 808 nm laser irradiation, enabling efficient synergy between high-contrast NIR-II FL imaging and high-performance PTT.[10,11] This study provides a new molecular design paradigm for developing high-performance NIR-II theranostic platforms through acceptor steric hindrance engineering.

EXPERIMENTAL

The experimental sections are described in the electronic supplementary information (ESI).

RESULTS AND DISCUSSION

Synthesis and Characterization of AIE-CPs

A series of CPs for NIR-II fluorescence imaging has been designed; however, the predominant nonradiative transitions resulted in almost complete quenching of their fluorescence. To explore the effect of receptor structural regulation on AIE, in this study, QIQ-2Sn was used as the donor unit, and BBT (benzothiadiazole, inner alkyl side chain of thiophene ring) and BBTD (benzothiadiazole derivative, outer alkyl side chain of thiophene ring) were used as receptors to synthesize two conjugated polymers, PBIQ and PBOQ, *via* the Stille coupling reaction (Fig. 1). Among them, 2-ethylpentanyl (inner alkyl chain) was introduced into the thiophene ring of BBT, while 2-octyldodecyl (outer alkyl chain) was adopted to regulate the molecular rigidity and aggregation behavior through the spatial positioning difference of the alkyl chains. The structures of both polymers were confirmed by ^{1}H-NMR spectroscopy, and the full spectra of PBIQ and PBOQ are shown in Figs. S1 and S2 (in ESI), respectively.

As shown in Fig. 2(a), PBIQ and PBOQ exhibited excellent solubility in tetrahydrofuran (THF) (1.0 mg/mL). Next, the absorption and emission spectra of the two polymers in THF were measured, and the absorption peaks of the two polymers were found to be in the range of 700–1000 nm (Fig. 2b). The main absorption peaks of PBIQ and PBOQ are located at 756 nm and 953 nm, respectively.[12]

As shown in Figs. 2(c) and 2(d), under the excitation of the 808 nm laser in THF solution, both CPs exhibited fluorescence emission at 850–1350 nm. The fluorescence emission peak of PBIQ in THF was 1286 nm and that of PBOQ was 965 nm, indicating that the introduction of an alkyl substituent on the receptor molecule enhanced the fluorescence intensity of the conjugated polymer to a certain extent.[13] At the same concentration, the emission intensity of PBIQ is 1.33 times than that of PBOQ. The extinction coefficients of PBIQ and PBOQ were calculated to be 1.45 and 2.04, respectively, at 808 nm (Fig. 2e). As shown in Fig. 2(f), the NIR-II fluorescence imaging results showed the strongest signal from PBIQ at the same concentration, which was consistent with previous testing. This further confirmed that the introduction of a side-chain non-conjugated functional group inside the receptor molecule could improve the emission of the near-infrared region of CPs.[14]

In studying the AIE effect, it was found that the photoluminescence (PL) intensity of PBIQ increased gradually with the increase of the water content in the THF/water mixture (Fig. 3a), and the fluorescence intensity of PBIQ increased from

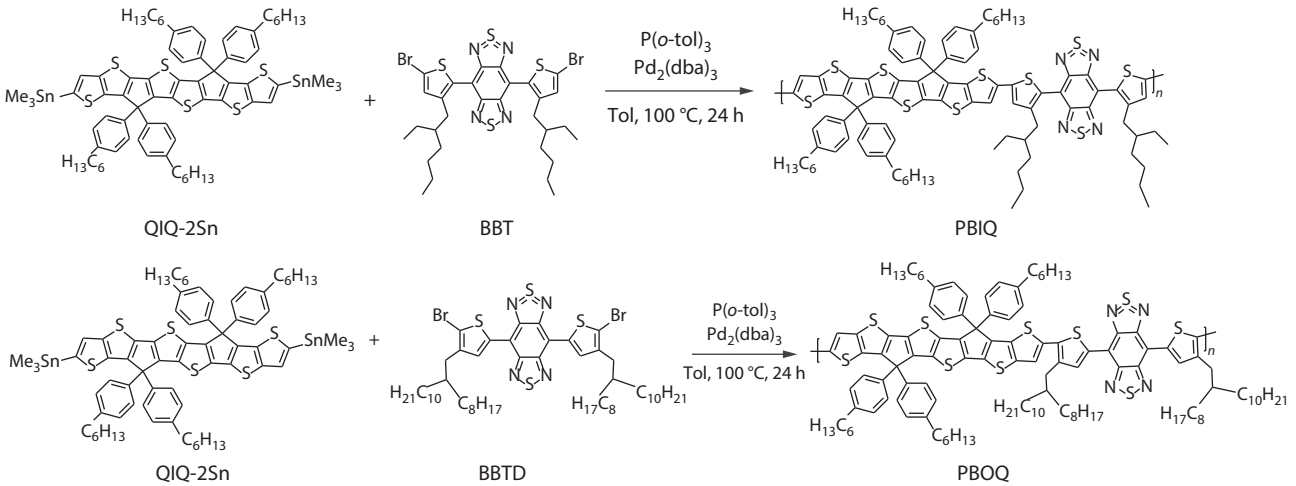


Fig. 1 Synthetic routes of the copolymers PBIQ and PBOQ.

36.96 to 42.66. PBIQ exhibited an optimal PL intensity at a 90 vol% water fraction. Compared with PBOQ, the PL intensity of PBOQ showed an irregular change of first increasing and then decreasing, and it was quenched significantly at 90 vol%,

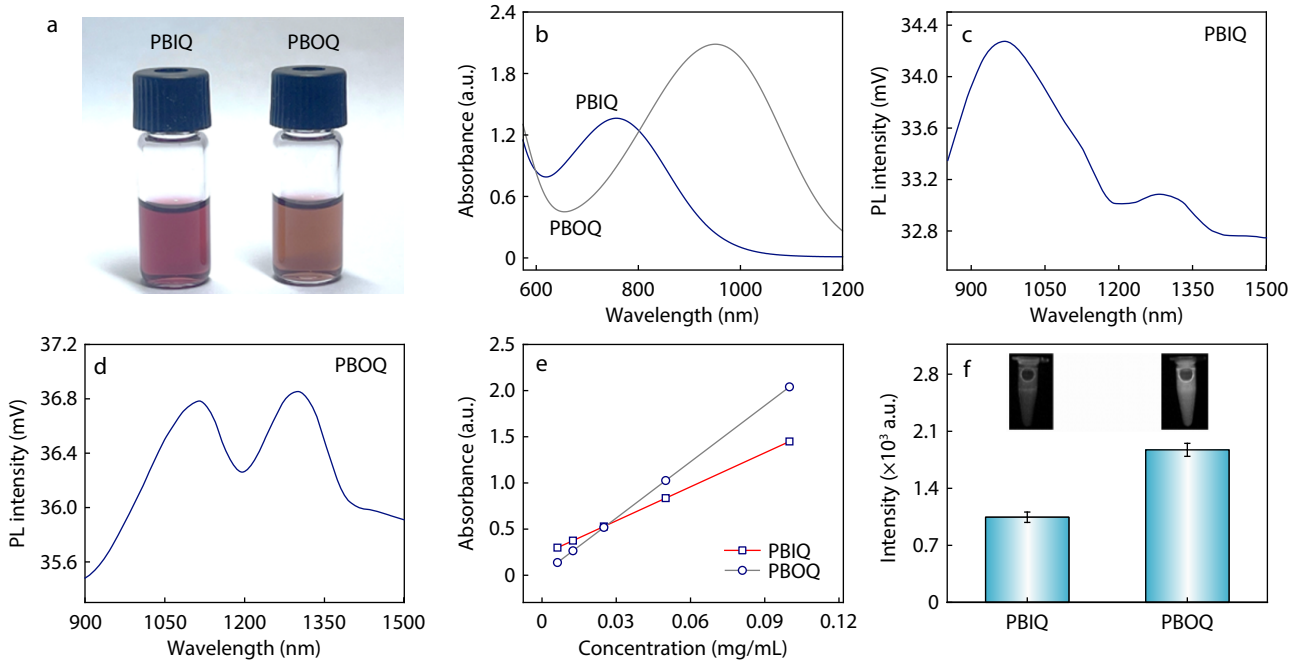


Fig. 2 Characterization of PBIQ and PBOQ in THF. (a) Image of the two products in THF (1.0 mg/mL); (b) Absorption spectra of PBIQ and PBOQ in THF solution; (c, d) Fluorescence emission spectra of PBIQ and PBOQ in THF solution; (e) Extinction coefficient of PBIQ and PBOQ; (f) NIR-II FL images and image intensities of the two products at an optical density of 1064 nm. Data are presented as mean ± standard deviation (SD), n=3 per group.

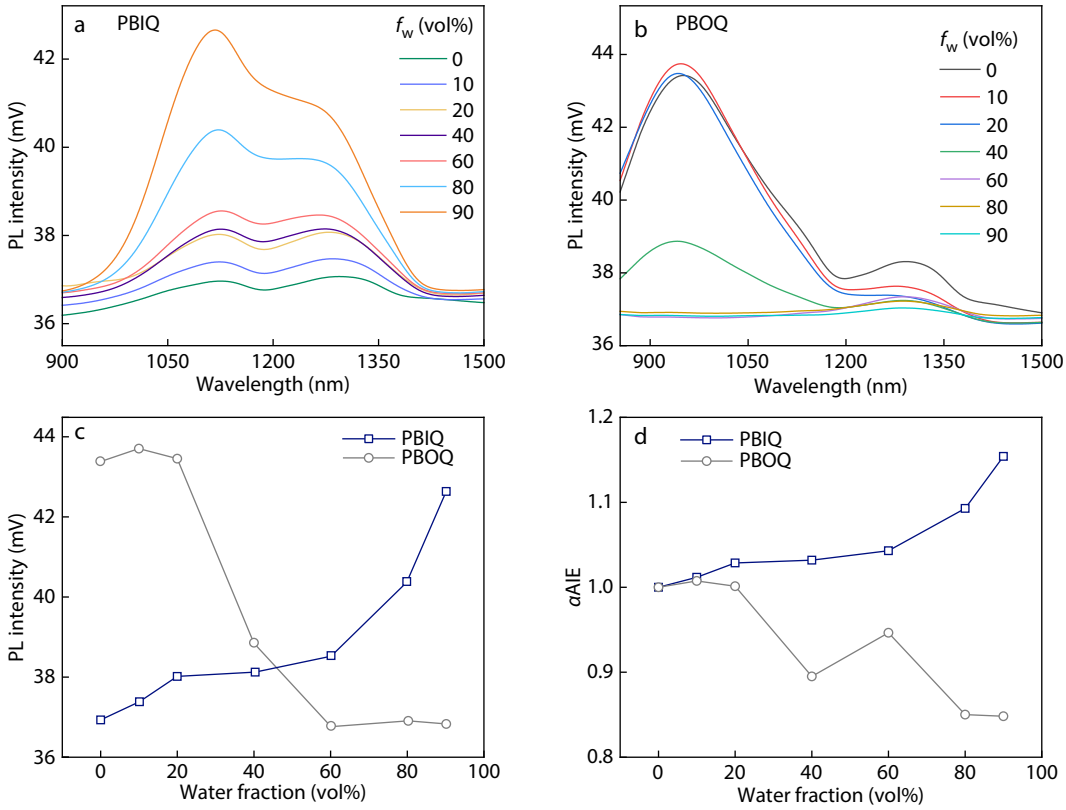


Fig. 3 Emission spectra of (a) PBIQ, (b) PBOQ in different THF and water (THF: water) at 808 nm; (c) Corresponding quantification of the aggregation-induced AIE effects of PBIQ NPs and PBOQ NPs; (d) Water fraction as a function of αAIE water/THF mixture.

https://doi.org/10.1007/s10118-026-3868-2

without the AIE effect (Fig. 3b). The structural comparison showed that the AIE effect was related to the side chain position of the AIE unit, and the internal side chain structure reduced the steric hindrance, thus reducing the resistance during molecular aggregation. In addition, the PL intensities of PBIQ and PBOQ at 90 vol% water fraction were 42.66 and 36.83, respectively (Fig. 3c). A comparison of the structures of PBIQ and PBOQ revealed that the increase in steric hindrance caused by the proximity of the alkyl chain to the benzothiazole plane resulted in an increase in the dihedral angle between the alkylthiophene and benzothiazole planes. This larger dihedral angle destroys the planarity of the polymer, resulting in a decrease in intermolecular π–π stacking and a decrease in the ACQ property[15](Fig. 3d).

Comparison of Water-soluble NPs

In addition, water-soluble NPs (*i.e.*, PBIQ and PBOQ NPs) were assembled using a nanoprecipitation method with amphiphilic Pluronic F-127. As shown in Fig. 4(a), PBIQ NPs and PBOQ NPs are dark purple and light purple (0.1 mg/mL), respectively. From the absorption spectra, the maximum absorption wavelengths of PBIQ and PBOQ are 817 and 982 nm, respectively (Fig. 4b). FL imaging in Figs. 4(c)–4(f) shows the strongest signal from PBIQ NPs, which is four times that of PBOQ NPs at the same concentration. Thus, the results for the water-soluble NPs were consistent with those for THF, further confirming the increase in steric hindrance caused by the internal alkyl chain to the benzothiazole plane, resulting in an increase in the dihedral angle between the alkylthiophene and benzothiazole planes.[16] This larger dihedral angle destroys the planarity of the polymer, resulting in less π-π stacking between the molecules and weaker ACQ properties. In addition, the particle size and morphology of the two types of CP NPs were characterized in detail using dynamic light scattering.

As can be seen from the results in Figs. 5(a) and 5(b), the hydrodynamic radii (<Dh>) of PBIQ NPs and PBOQ NPs are 91.8 and 76.5 nm, respectively, with a narrow particle size distribution. Meanwhile, the PBIQ NPs exhibited spherical morphology and favorable monodispersity (Fig. 5c). The long-term storage stability of both PBIQ and PBOQ NPs over 3, 7, and 15 days is further demonstrated in Fig. S2 (in ESI), which confirms that the as-prepared nanoparticles possess satisfactory colloidal stability under storage conditions. Both polymers exhibited excellent light absorption at 808 nm, and their photothermal properties in aqueous solutions were further studied.[17] First, the photothermal properties of the two solutions were tested in a centrifuge tube with 808 nm excitation light at a power of 1.0 W/cm^2. Real-time capture of temperature changes using thermal imagers. As shown in Fig. 5(d), the temperature of PBIQ NPs and PBOQ NPs increased to 51.6 and 51.3 °C, respectively, at a concentration of 0.1 mg/mL.[18] The maximum temperature of the PBIQ NPs increased significantly with an increase in power density. As shown in Fig. 5(e), the maximum temperature reached by the PBIQ NPs solution increased with an increase in the solution concentration at a given laser power density. The temperature curve shows that when the concentration of PBIQ NPs is 0.1 mg/mL, the temperature increases to 51.6 °C and the maximum temperature difference is 27.3 °C within 5 min after irradiation. In contrast, pure water irradiated with 808 nm laser can only reach 30.1 °C, with a temperature difference within 10 °C, which is about five times the increased temperature of pure

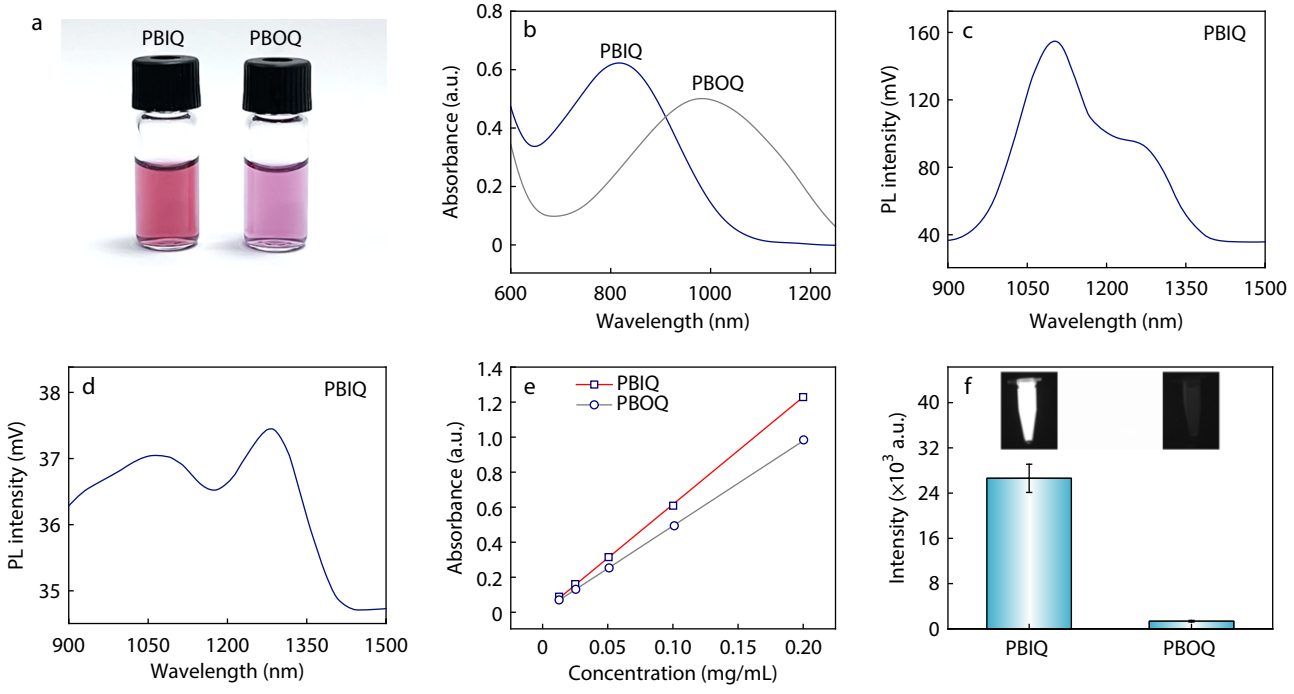


Fig. 4 Characterization of PBIQ NPs and PBOQ NPs in water. (a) Image of the two products in water (1.0 mg/mL); (b) Absorption spectra; (c, d) Emission spectra; (e) The extinction coefficient of the two nanoparticles (the corresponding absorption spectrum is shown in Fig. 3b); (f) NIR-II FL image and image intensity of the two nanoparticles at an optical density of 1064 nm. Data are presented as mean ± standard deviation (SD), n=3 per group.

https://doi.org/10.1007/s10118-026-3868-2

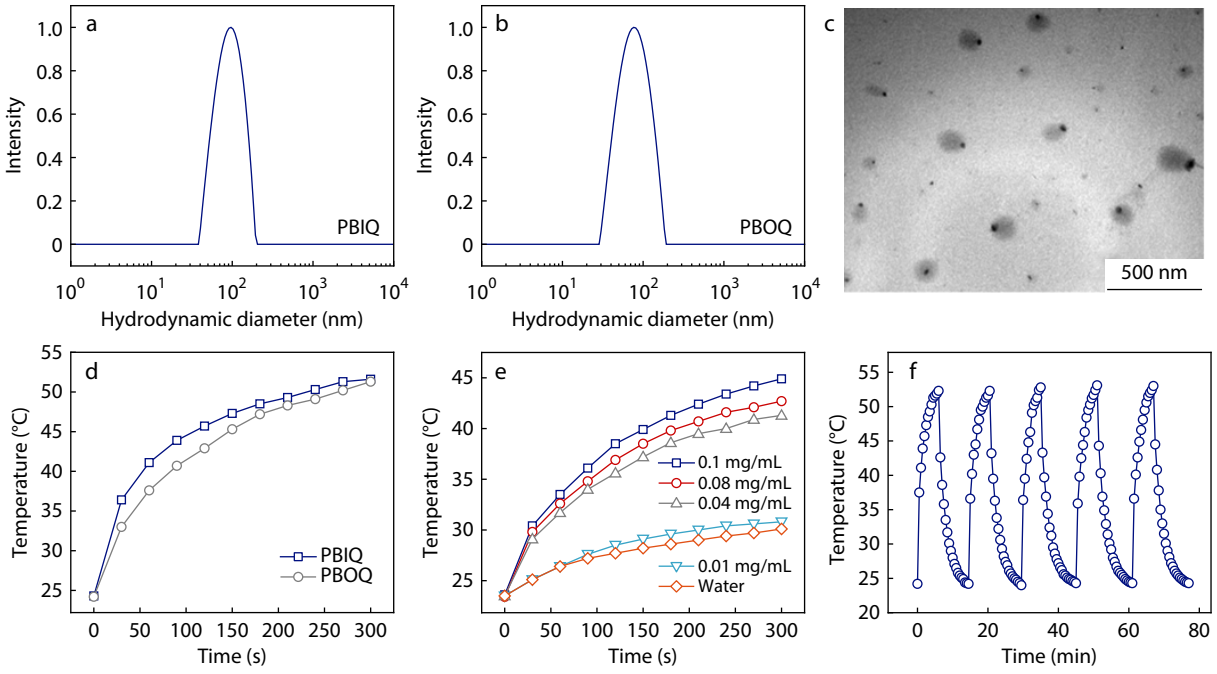


Fig. 5 (a, b) Mean hydrodynamic diameters of PBIQ NPs, PBOQ NPs using DLS; (c) Transmission electron microscope (TEM) image of PBIQ NPs; (d) The heating curves of PBIQ NPs and PBOQ NPs aqueous solutions irradiated with a laser at 808 nm for 5 min (1.0 mg/mL, 1.0 W/cm^2); (e) The temperature rise curve of different concentrations of PBIQ NPs aqueous solution with irradiation time under 808 nm light (1.0 W/cm^2); (f) The temperature change curve of PBIQ NPs in 5 cycles.

water under the same conditions. These results indicate that PBIQ NPs exhibit excellent photothermal conversion at 808 nm excitation, making them potentially useful for PTT applications. Subsequently, PBIQ NPs were subjected to multiple cycles of light irradiation with little change in the maximum temperature after laser irradiation, indicating the good photothermal stability of PBIQ NPs (Fig. 5f).[19] This further supports their potential application for PTT *in vivo*. A PBIQ NPs photothermal conversion efficiency of 70.51% was calculated based on the solution cooling curve. Therefore, PBIQ NPs provide superior imaging of the NIR-II FL compared to PBOQ under excitation at 808 nm,which can be attributed to acceptor-side- chain-induced steric hindrance that disturbs backbone planarity, suppresses intermolecular π-π stacking, and alleviates the ACQ effect. PBIQ NPs were selected as the optical diagnostic reagent for subsequent studies, and NIR-II FL-guided PTT has great application prospect.[20]

PBIQ Cell Experiment

The uptake behavior of PBIQ nanoparticles in 4T1 cells was investigated prior to the subsequent cellular and *in vivo* experiments. After incubation for 0, 1, 8, and 12 h, the fluorescence intensity was detected using the NIR-II imaging system.[13] As shown in Fig. 6(a), the fluorescence intensity was highest at 12 h, indicating that cell uptake was the strongest at that time point. Next, the cytotoxicity of PBIQ NPs against 4T1 mouse cancer cells was evaluated using the 3-(4,5-dimethylthiazole-2-yl)-2,5-diphenylbromotetrazole (MTT) assay.

Cytotoxicity of PBIQ NPs in 4T1 mouse cancer cells. A series of concentration-gradient aqueous solutions of PBIQ NP were prepared and co-cultured with 4T1 cells for 24 h. As shown in Fig. 6(b), in the absence of laser irradiation, even cells treated with high concentrations of PBIQ (100 mg/mL) were able to maintain their cell viability above 90% and did not exhibit significant changes with increasing concentration, indicating that PBIQ NPs caused less cell damage and were therefore safe for *in vivo* applications.[21] After the cultured 4T1 cells were irradiated with an 808 nm laser (1.0 W/cm^2) for 5 min, they were found to have gradually decreased cell viability with an increase in PBIQ concentration. When the NPs concentration was 0.1 mg/mL, only about 7.94% of the 4T1 cells survived, indicating that the nanomaterial had significant phototherapy effect on tumor cells under laser irradiation. To further quantify the apoptosis induced by photothermal treatment, Annexin V-FITC/PI staining was performed for flow cytometric analysis.[22] As shown in Fig. 6(c), the survival rate of 4T1 cells incubated with PBIQ nanoparticles and subjected to laser irradiation was less than 9%, confirming that laser irradiation with PBIQ NPs induced apoptosis. These *in vitro* experimental results showed that PBIQ nanoparticles had an excellent antitumor photothermal treatment effect under laser irradiation at 808 nm.[23]

NIR-II Fluorescence Imaging of PBIQ NPs

After the injection of PBIQ NPs (1.0 mg/mL, 150 μL) through the caudal vein in a 4T1 tumor-bearing mouse model, timing monitoring was performed using a NIR-II fluorescence imaging system with 808 nm excitation light and a 1064 nm long-pass filter,[24] as shown in Fig. 7(a). The results showed that specific fluorescence signals began to appear in the tumor area 4 h after injection, and the signal strength continuously increased with time, reaching a peak at 24 h (approximately six times higher than the initial 0.1-h signal strength)[25] (Fig. 7b). This time point, corresponding to the maximum enrichment of

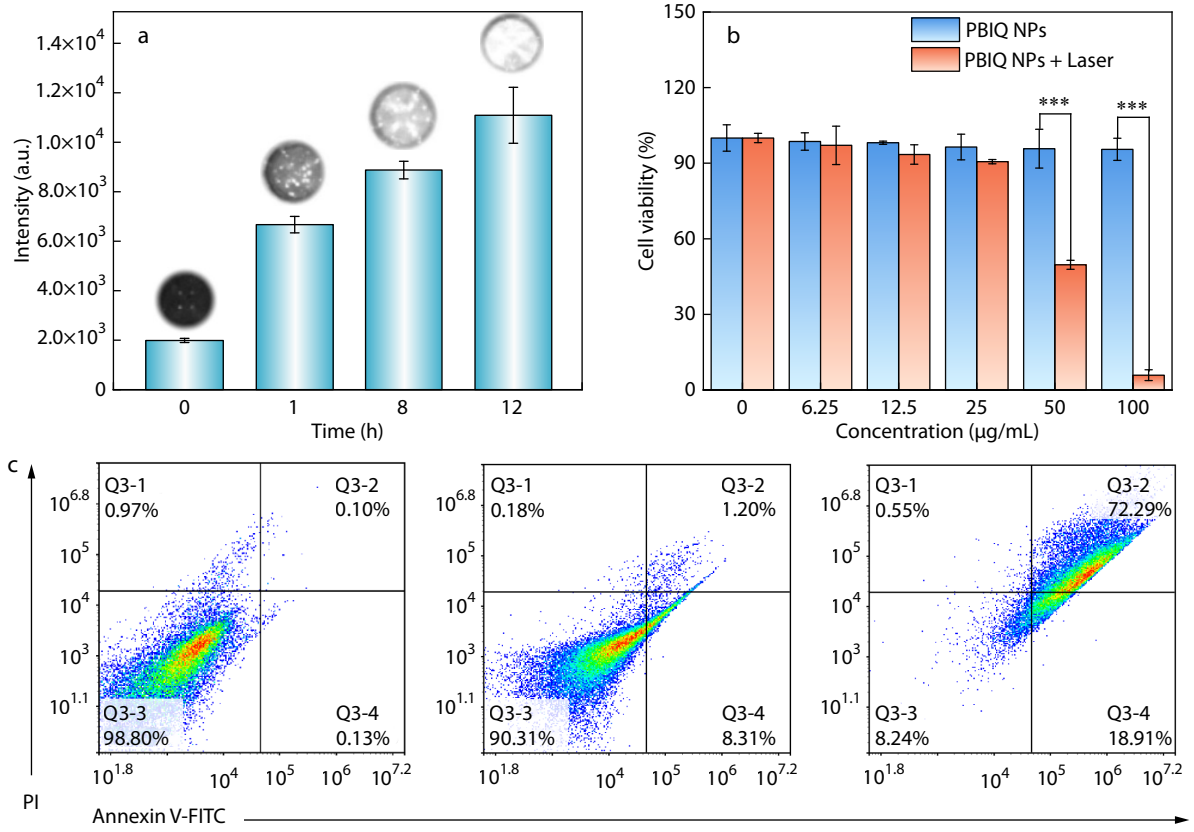


Fig. 6 PTT of PBIQ NPs on 4T1 cells. (a) NIR-II FL images and quantitative fluorescence intensity for different time periods when PBIQ NPs were co-cultured with 4T1 cells; (b) Survival rate of 4T1 cells after different treatments. The 4T1 cells were incubated with different concentrations of PBIQ NPs under 808nm laser irradiation (5 min, 1.0 W/cm^2). The levels of statistical significance were categorized as $^*P < 0.05$, $^{**}P < 0.01$, and $^{***}P < 0.001$. (c) Flow cytometry apoptosis analysis of 4T1 cells after different treatments using Annexin V-FITC/PI staining: control, PBIQ NPs, PBIQ NPs + 808 nm laser.

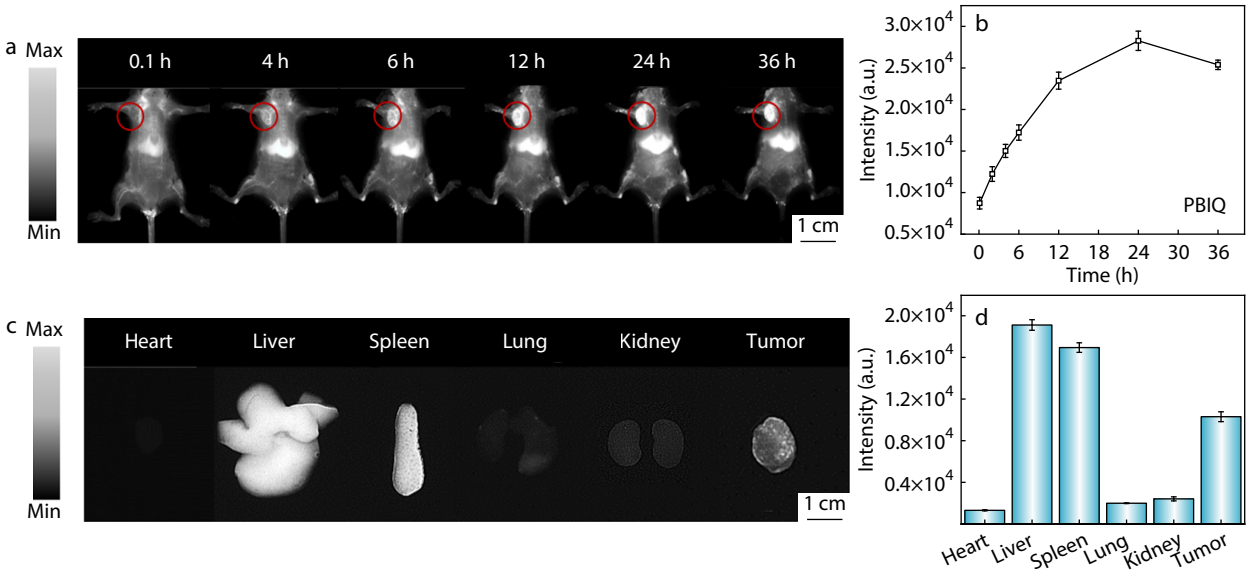


Fig. 7 *In vivo* NIR-II FL image of a mouse carrying 4T1. (a) NIR-II FL imaging of tumor-bearing mice (tumor sites are indicated by red dashed circles (scale bar: 1 cm)); (b) The change of NIR-II FL intensity in tumor-bearing mice with the injection time of PBIQ NPs; (c) *In vitro* NIR-II FL images 36h after intravenous administration of PBIQ NPs (scale bar: 1 cm) and (d) signal strength of heart, liver, spleen, lungs, kidneys and tumors. Data are presented as mean ± standard deviation (SD), n=3 per group.

nanoparticles at the tumor site, was the optimal time window of 15 for photothermal therapy. During this process, PBIQ NPs demonstrated high spatial resolution imaging characteristics (FWHM of the half-maximum width of the blood vessel ≈

0.25–0.29 mm) and excellent signal-to-noise ratio (SBR>8), which is significantly superior to the traditional NIR-I probe because of its effective suppression of scattering by biological tissues in the emission band of 1200–1400 nm. The tumor fluorescence intensity gradually declined because of metabolic clearance at 33 h after injection (Fig. 7c). Imaging of isolated organs further confirmed that after 36 h, the fluorescence signals were mainly enriched in the liver (accounting for 68%±5% of the total), followed by the spleen (21%±3%), as shown in Fig. 7(d), indicating that they passed through the metabolic pathway dominated by the hepatobiliary system, consistent with the metabolic characteristics of similar conjugated polymer nanoprobes.[26] The above results not only highlight the ability of PBIQ NPs to achieve precise treatment guided by high-contrast NIR-II imaging but also clarify the correlation between metabolic kinetics and treatment time window, providing the basis for key parameters for clinical transformation.[27]

CONCLUSIONS

In this study, a conjugated polymer, PBIQ, with AIE, was designed and synthesized by a Stille coupling reaction. By introducing a sterically hindered side chain and embedding a flexible non-conjugated alkyl chain in the receptor unit, the dihedral angle of the polymer main chain is effectively increased, and the ACQ effect induced by π-π stacking is significantly inhibited; thus, the material is endowed with excellent AIE activity. The maximum fluorescence emission wavelength of PBIQ NPs was extended to 1062 nm, confirming efficient NIR-II fluorescence emission *via* AIE unit modulation. Among them, PBIQ NPs exhibit excellent properties, such as good water solubility, remarkable AIE characteristics (αAIE=1.15), up to 70.51% photothermal conversion efficiency (808 nm), and excellent biocompatibility. *In vitro* experiments showed that PBIQ NPs efficiently ablated tumor cells. The spatial steric hindrance regulation strategy proposed in this work not only solves the problem of radiation/non-radiation transition imbalance of conjugated polymers but also provides a new idea for the design of an integrated reagent that combines high-sensitivity NIR-II imaging with high-efficiency photothermal therapy, and is expected to promote the clinical transformation of the diagnosis and treatment of integrated materials for precise tumor treatment.

Conflict of Interests

The authors declare no interest conflict.

Electronic Supplementary Information

Electronic supplementary information (ESI) is available free of charge in the online version of this article at http://doi.org/10.1007/s10118-026-3868-2.

Data Availability Statement

The related data for this paper (DOI: 10.57760/sciencedb.011zi) are available in the Science Data Bank (ScienceDB) database at https://www.scidb.cn/anonymous/ZmVpNmZx.

ACKNOWLEDGMENTS

This work was financially supported by the National Natural Science Foundation of China (Nos. 22375102, 2373142 and U24A2077).

REFERENCES

1 Wan, Y.; Gao, Y.; Chen, Y. N.; Lee, K. W.; Wang, H. W.; Tsai, Y. J.; Chen, W.; Li, S.; Wong, K. T.; Lee, C. S. Achieving high-brightness NIR-II emission: molecular locking and wrapping strategies in fluorescent material design for *in vivo* bioimaging. *Adv. Mater.* **2025**, *37*, e10386.
2 Dai, Y.; Zhang, F.; Chen, K.; Sun, Z.; Wang, Z.; Xue, Y.; Li, M.; Fan, Q.; Shen, Q.; Zhao, Q. An activatable phototheranostic nanoplatform for tumor specific NIR-II fluorescence imaging and synergistic NIR-II photothermal-chemodynamic therapy. *Small* **2023**, *19*, 2207053.
3 Liu, Y.; Zhang, Z.; Hou, X.; Ding, Q.; Zeng, S.; Shen, H.; Gong, W.; Ding, T.; Mahmood, Z.; Zeng, X.; Ren, B.; Hu, W.; Hong, X.; Ding, D.; Xiao, Y. Aggregation-mediated photoacoustic/NIR-II and photodynamic properties of pH-reversible thiopyrylium agents: a computational and experimental approach. *Adv. Mater.* **2025**, *37*, 2420006.
4 Park, H. B.; An, E. K.; Kim, S. J.; Ryu, D.; Zhang, W.; Pack, C. G.; Kim, H.; Kwak, M.; Im, W.; Ryu, J. H.; Lee, P. C. W.; Jin, J. O. Anti-PD-L1 antibody fragment linked to tumor-targeting lipid nanoparticle can eliminate cancer and its metastasis *via* photoimmunotherapy. *ACS Nano* **2024**, *18*, 33366–33380.
5 Xu, L.; Zhang, Q.; Wang, X.; Lin, W. Biomedical applications of NIR-II organic small molecule fluorescent probes in different organs. *Coord. Chem. Rev.* **2024**, *519*, 216122.
6 Liu, H.; Gao, C.; Xu, P.; Li, Y.; Yan, X.; Guo, X.; Wen, C.; Shen, X. C. Biomimetic gold nanorods-manganese porphyrins with surface-enhanced Raman scattering effect for photoacoustic imaging-guided photothermal/photodynamic therapy. *Small* **2024**, *20*, 2401117.
7 Miao, X.; Jia, M.; Weng, X.; Zhang, J.; Pan, Y.; Zhao, H.; Yu, Z.; Fan, Q.; Hu, W. Alleviating NIR-II emission quenching in ring-fused fluorophore *via* manipulating dimer populations for superior fluorescence imaging. *Light Sci. Appl.* **2025**, *14*, 109.
8 Mu, J.; Xiao, M.; Shi, Y.; Geng, X.; Li, H.; Yin, Y.; Chen, X. The chemistry of organic contrast agents in the NIR-II window. *Angew. Chem. Int. Ed.* **2022**, *61*, e202114722.
9 Hu, X.; Fang, Z.; Zhu, C.; Yang, Y.; Yang, Z.; Huang, W. Crucial breakthrough of BODIPY-based NIR-II fluorescent emitters for advanced biomedical theranostics. *Adv. Funct. Mater.* **2024**, *34*, 2401325.
10 Liu, X.; Yu, B.; Shen, Y.; Cong, H. Design of NIR-II high performance organic small molecule fluorescent probes and summary of their biomedical applications. *Coord. Chem. Rev.* **2022**, *468*, 214609.
11 Yang, X.; Wang, X.; Zhang, X.; Zhang, J.; Lam, J. W. Y.; Sun, H.; Yang, J.; Liang, Y.; Tang, B. Z. Donor–acceptor modulating of ionic AIE photosensitizers for enhanced ROS generation and NIR-II emission. *Adv. Mater.* **2024**, *36*, 2402182.
12 Wei, M.; Bai, J.; Shen, X.; Lou, K.; Gao, Y.; Lv, R.; Wang, P.; Liu, X.; Zhang, G. Glutathione-exhausting nanoprobes for NIR-II fluorescence imaging-guided surgery and boosting radiation therapy efficacy *via* ferroptosis in breast cancer. *ACS Nano* **2023**, *17*, 11345–11361.
13 Wilson, B. E.; Wright, K.; Koven, R.; Booth, C. M. Surveillance imaging after curative-intent treatment for cancer: benefits, harms, and evidence. *J. Clin. Oncol.* **2024**, *42*, 2245–2249.
14 Zhong, Y. H.; Huang, G. F.; Zhao, S. Y.; Chung, L. H.; Zhang, H. T.;

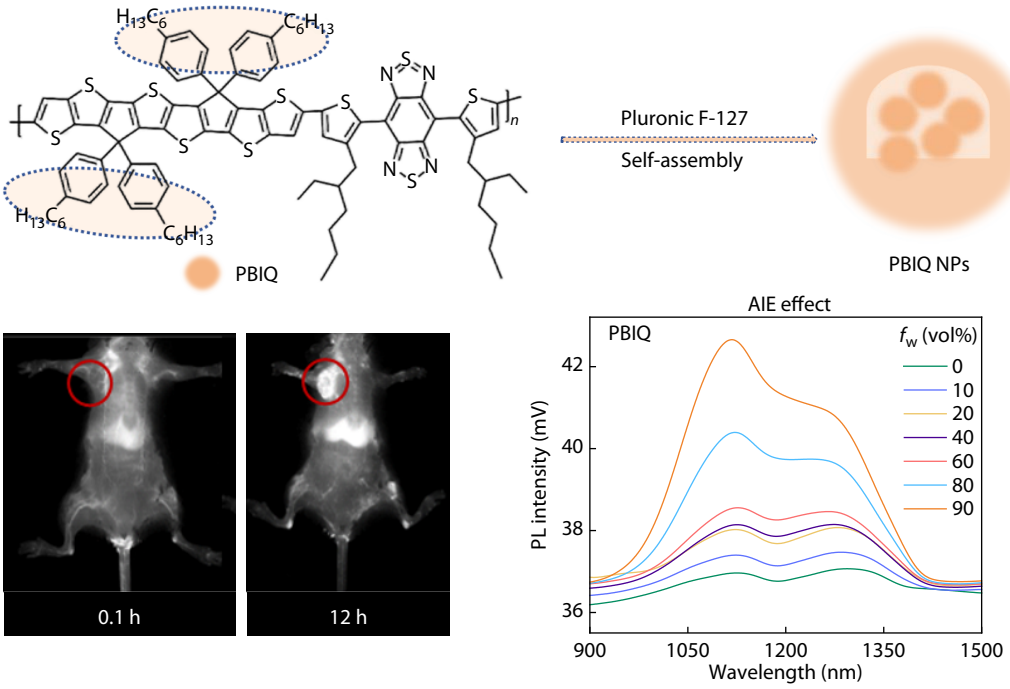
Graphical Abstract

Leveraging Steric Hindrance Engineering in Conjugated Polymers for Enhanced NIR-II Fluorescence Imaging and High-efficiency Photothermal Therapy

Bin Chang, Chen-Hang Xi, Zi-Kun Yu, Zi-Xin Hu, Peng-Fei Chen, Qu-Li Fan, and Peng-Fei Sun

Nanjing University of Posts & Telecommunications; Huangshan University; Nanjing University

An aggregation-induced emission (AIE)-active nanoplatform (PBIQ NPs) was constructed *via* regulation of steric hindrance for integrated the second near-infrared (NIR-II) phototheranostics. This enables precise tumor diagnosis using high-performance NIR-II fluorescence imaging. Upon 808 nm laser irradiation, ultrahigh photothermal conversion (70.51%) was achieved, driving highly efficient tumor ablation with excellent biocompatibility.



Chinese J. Polym. Sci. 2026 *https://doi.org/10.1007/s10118-026-3868-2*

Zheng, J. H.; Yan, Y. L.; Ni, W. X.; He, J. Easy but efficient: facile approach to molecule with theoretically justified donor-acceptor structure for effective photothermal conversion and intravenous photothermal therapy. *Adv. Sci.* **2024**, *11*, e2309068.

15 Du, Y.; Ni, S.; Ma, Q.; Song, X.; Yang, H. Engineering NIR-II luminescent lanthanide nanoprobes for imaging brain diseases *in vivo*. *Coord. Chem. Rev*. **2023**, *496*, 215401.

16 Sun, J.; Cheng, W.; Liu, X.; Xiang, H.; Ruan, C.; Chen, F.; Yao, C. Gold clusters: a promising NIR-II probe for bioimaging and biosensing. *Coord. Chem. Rev.* **2025**, *533*, 216544.

17 Li, C.; Du, J.; Jiang, G.; Gong, J.; Zhang, Y.; Yao, M.; Wang, J.; Wu, L.; Tang, B. Z. White-light activatable organic NIR-II luminescence nanomaterials for imaging-guided surgery. *Nat. Commun.* **2024**, *15*, 5832.

18 Zhen, S.; Xu, Z.; Suo, M.; Zhang, T.; Lyu, M.; Li, T.; Zhang, T.; Li, M.; Zhao, Z.; Tang, B. Z. NIR-II AIE liposomes for boosting type-I photodynamic and mild-temperature photothermal therapy in breast cancer treatment. *Adv. Mater.* **2025**, *37*, 2411133.

19 Liu, C.; Cai, Y.; Zhang, Z.; Lu, Y.; Zhu, Q.; He, H.; Chen, Z.; Zhao, W.; Wu, W. Julolidinyl aza-BODIPYs as NIR-II fluorophores for the bioimaging of nanocarriers. *Acta Pharm. Sin. B* **2024**, *14*, 3155−3168.

20 Li, B.; Zhao, M.; Lin, J.; Huang, P.; Chen, X., Management of fluorescent organic/inorganic nanohybrids for biomedical applications in the NIR-II region. *Chem. Soc. Rev*. **2022,** *51*, 7692-7714.

21 Chen, J. N.; Huang, K. X.; Cheng, P. M.; Qi, M. Q.; Xu, H.; Chen, J.; Duan, Y.; Kong, X. J.; Zheng, L. S.; Long, L. S. Strong NIR-II magneto-optical activity of a chiral $Sm_{15}Cu_{54}$ cage. *J. Am. Chem. Soc.* **2024**, *146*, 22913−22917.

22 Roy, S.; Bag, N.; Bardhan, S.; Hasan, I.; Guo, B. Recent progress in NIR-II fluorescence imaging-guided drug delivery for cancer theranostics. *Adv. Drug Deliv. Rev.* **2023**, *197*, 114821.

23 Li, D.; Deng, X.; Xu, Z.; Wang, D.; Xu, G.; Zhang, P.; Qiu, P.; Xie, W.; Wang, D.; Tang, B. Z.; Wang, K. Molecular engineering of NIR-II AIE luminogen excited at 1700 nm for ultradeep intravital brain

two-photon fluorescence imaging. *Adv Funct Mater* **2023**, *33*, 2303967.
24 Guo, S.; Tang, D.; Zhang, M.; Yang, H.; Zhang, T.; Hu, B.; Xu, C.; Weng, Y.; Shang, K.; Huang, Y. Spatiotemporal-controlled NIR-II immune agonist sensitizes cancer immunotherapy. *Adv. Mater.* **2024**, *36*, 2400228.
25 Sun, Y.; Sun, P.; Li, Z.; Qu, L.; Guo, W. Natural flavylium-inspired far-red to NIR-II dyes and their applications as fluorescent probes for biomedical sensing. *Chem. Soc. Rev.* **2022**, *51*, 7170–7205.
26 Yang, M.; Yang, C.; Wei, G.; Tan, W.; Ji, D. K. NIR-II emitting fluorine-doped carbon dots with multi-enzyme mimic activities for NIR-II imaging and photothermal-enhanced cancer catalytic immunotherapy. *Carbon* **2025**, *243*, 120533.
27 Yan, D.; Li, Z.; Lee, M. M. S.; Tang, B.; Wang, D. NIR-II AIEgens for infectious diseases phototheranostics. *Angew. Chem. Int. Ed.* **2024**, *63*, e202414259.

https://doi.org/10.1007/s10118-026-3868-2